Theor. Comput. Fluid Dyn.
DOI 10.1007/s00162-010-0199-1

ORIGINAL ARTICLE

Philipp Schlatter · Shervin Bagheri · Dan S. Henningson

Self-sustained global oscillations in a jet in crossflow

Received: 1 June 2009 / Accepted: 12 January 2010

Abstract A jet in crossflow with an inflow ratio of 3, based on the maximum velocity of the parabolic jet profile, is studied numerically. The jet is modeled as an inhomogeneous boundary condition at the crossflow wall. We find two fundamental frequencies, pertaining to self-sustained oscillations in the flow, using full nonlinear direct numerical simulation (DNS) as well as a modal decomposition into global linear eigenmodes and proper orthogonal decomposition (POD) modes; a high frequency which is characteristic for the shear-layer vortices and the upright vortices in the jet wake, and a low frequency which is dominant in the region downstream of the jet orifice. Both frequencies can be related to a region of reversed flow downstream of the jet orifice. This region is observed to oscillate predominantly in the wall-normal direction with the high frequency, and in the spanwise direction with the low frequency. Moreover, the steady-state solution of the governing Navier–Stokes equations clearly shows the horseshoe vortices and the corresponding wall vortices further downstream, and the emergence of a distinct counter-rotating vortex pair high in the free stream. It is thus found that neither the inclusion of the jet pipe nor unsteadiness is necessary to generate the characteristic counter-rotating vortex pair.

Keywords Jet in crossflow · Global instabilities · Proper orthogonal decomposition · Elliptic instability

1 Introduction

A large number of studies have been devoted to the flow case of a jet in crossflow, not only due to its technical relevance in, for example film, cooling, fuel injection, etc., but also dispersion of pollutants from e.g., smoke-stacks or in assessing V/STOL airplanes. The flow structures, mixing properties, and complex dynamics have, therefore, been studied extensively by means of experiments and—more recently—by computer simulations. In general, four main coherent structures (see e.g. [12,15,22,27,29,33,37] and references therein) characterize the jet in crossflow: (i) the counter-rotating vortex pair which is thought to originate in the near field and remains the most dominant structure of the flow field far downstream; (ii) the shear-layer vortices which initially take the form of ring-like or loop-like shapes and cause the jet to disintegrate into smaller vortices; (iii) the horseshoe vortices formed upstream of the jet nozzle, and their extension downstream of the nozzle, usually termed wall vortices; and (iv) the upright vortices populating the jet wake in between the jet trajectory and the flat plate. Depending on the exact parameter settings (boundary-layer thickness, jet radius and inflow profile, jet speed, turbulence levels in crossflow and pipe, etc.), the specific characteristics and relative importance of the above main structures might vary considerably (see e.g. [15]).

Communicated by T. Colonius

P. Schlatter · S. Bagheri (✉) · D. S. Henningson
Linné Flow Centre, KTH Mechanics, 100 44 Stockholm, Sweden
E-mail: shervin@mech.kth.se

Published online: 14 April 2010

Traditionally, the studies of the jet in crossflow have been concerned with the location and scaling of the centerline trajectory, the mean and fluctuating velocity properties and the mixing properties at various jet-to-crossflow ratios R. Despite the large number of studies, there are still a number of open questions related to more fundamental issues: the dominant mechanism for the generation of e.g., the counter-rotating vortex pair [12,22,29], or the upright vortices and their relation to the observed low-frequency wiggling of the whole jet configuration that are of interest [15]. Moreover, there is a lack of consensus of the origin of the shear-layer vortices. Numerous studies argue that the main instability mechanism is of Kelvin–Helmholtz (KH) type due to the shearing between the jet and the main stream (see e.g. [22]), whereas other studies [9] indicate that the elliptic instability of the steady longitudinal counter-rotating vortex pair must be taken into account when describing the instability mechanisms of the jet. As we discuss in this article, both of these physical mechanisms could be present at the same time and the resulting combined *global* instability dynamics should be considered.

Supporting evidence that the jet in crossflow is able to self-sustain global oscillations was provided by Megerian et al. [27] by analyzing single-point spectral data. They found the spectrum peaks rather insensitive to periodic forcing when $R < 3$. The same self-sustained oscillatory behavior have been observed in other experiments [9], and also in the study by Kelso et al. [22] where the frequency of the shear-layer instability could not be affected via forcing close to the jet nozzle. However, to ascertain that a flow exhibits self-sustained oscillatory behavior via a bifurcation, a global instability in time from its inception through its small-amplitude linear stage to saturation has to be traced to evaluate the coefficients of the Landau equation. Such a study remains to be undertaken for the jet in crossflow. A related, but certainly easier and more feasible task is a linear global stability analysis of a steady solution at a single velocity ratio; in case of a global instability, the steady solution will give rise to a coherent array of vortex structures which oscillate with the frequency of the global modes. However, the nonlinear saturation of the unstable modes and the ultimate nonlinear shedding frequencies cannot be determined by the linear analysis. Note that for highly unsteady flows, such an analysis can only be performed numerically, since the flow never visits unstable equilibria; one observes only the nonlinear dynamics on attractors, resulting from the global instability.

Recently, Bagheri et al. [6] performed the first linear global stability analysis of a steady solution of the jet in crossflow at $R = 3$ using a numerical simulations in conjunction with iterative techniques. They found a number of unstable linear global modes; high frequency modes were predominantly located on the jet trajectory and low-frequency modes near the wall region downstream of the jet nozzle. The global analysis suggests that the jet in crossflow may exhibit self-sustaining global oscillations. Indeed, time series of probes of DNS calculations showed two fundamental frequencies; one high frequency oscillations associated to unsteady jet shear-layer vortices and one with low frequency associated with oscillating wall structures.

This study aims at further characterizing the self-sustained oscillatory behavior of the jet in crossflow at $R = 3$. In particular, the following goals are set:

(a) A new nonlinear DNS data set with long time history has been computed where asymmetric flow structures have been initially triggered (in the previous DNS by Bagheri et al. [6] the spanwise symmetry was sustained for all times). The symmetric and anti-symmetric data are compared to identify if asymmetry is a necessary ingredient for vortex shedding.
(b) The various steady flow structures of the jet in crossflow, i.e., the two distinct nearly longitudinal vortex tubes (counter-rotating vortex pair, CVP), the shear layer and separated regions of the steady solution, are discussed and compared the time-averaged mean flow.
(c) The relation of the unstable global modes to Kelvin–Helmholtz instability, elliptic type of instabilities and the unsteady separated region are discussed qualitatively.
(d) The fundamental frequencies of the flow are associated to the most energetic global structures in the flow obtained via proper orthogonal decomposition (POD).

The study of a jet in crossflow is challenging for experimental as well as numerical study. The flow is always fully three-dimensional and spatially developing, proper inflow conditions need to be specified for both the crossflow boundary layer and the jet exit, and the various shedding frequencies in the flow call for long observation times. Numerically, the jet in crossflow has been initially studied via large-eddy simulation (LES) by Yuan et al. [37], where the authors could find reasonable agreement with experiments performed with similar parameters, and a first classification of the flow structures could be performed. A series of well-resolved direct numerical simulations (DNS) of a round jet in crossflow has been performed recently by Muppidi and Mahesh [28,30] using a turbulent inflow. In particular, new scaling laws for the jet trajectories were proposed, and extensive budgets of turbulent quantities could be provided. Using an alternative simulation approach based on vortex elements, Cortelezzi and Karagozian [12] studied the development of the counter-rotating vortex pair and the near field of the jet in detail.

In this study, we employ a fully spectral numerical method, naturally limiting the geometrical flexibility of the simulation setup. In particular, we chose to enforce the jet as a steady Dirichlet boundary condition on the crossflow wall, as opposed to e.g., Yuan et al. [37] or Muppidi and Mahesh [28,30], see also the discussion in Sect. 2 further below. However, the aim here is to contribute to a more fundamental understanding of the jet dynamics rather than providing additional data points for e.g., the trajectory development at certain parameters. Nevertheless, the complexity of the flow demands a large number of degrees of freedom for any fully-resolved numerical simulation. Therefore, in addition to traditional (linear and nonlinear) DNS, we apply for the computation of the steady solution and the global modes methods based on time-steppers, i.e., at no point, a full matrix of the evolution operator is explicitly built as its size would be impractical.

The article is organized as follows. Section 2 introduces the numerical setup together with the simulation method employed for this study and the specific parameter settings. A characterization of the steady and unsteady flow features are given in Sect. 3. The steady and oscillatory behavior of separated regions in the flow are studied in Sect. 4. In Sect. 5 a global modal analysis of the flow is presented, both in terms of (linear) global eigenmodes and (nonlinear) modes from proper orthogonal decomposition (POD). Conclusions and an outlook are given in Sect. 6.

2 Numerical methods and parameters

2.1 Simulation set-up

The simulation code (see [10]) employed for the direct numerical simulations presented in this article uses spectral methods to solve the three-dimensional, time-dependent, incompressible Navier–Stokes equations over a flat plate. The streamwise, wall-normal, and spanwise directions are denoted by x, y, and z, respectively, and the corresponding velocity vectors are $\boldsymbol{u} = (u, v, w)^T$,

$$\frac{\partial \boldsymbol{u}}{\partial t} + (\boldsymbol{u} \cdot \nabla)\boldsymbol{u} = -\nabla p + \frac{1}{Re_{\delta_0^*}} \nabla^2 \boldsymbol{u} + F(\boldsymbol{u}), \tag{2.1}$$

$$\nabla \cdot \boldsymbol{u} = 0, \tag{2.2}$$

with the pressure p. The volume forcing $F(\boldsymbol{u})$ pertaining to the fringe region is described further below. The algorithm is based on Fourier discretization in the streamwise and spanwise directions, and the wall-normal direction is expanded in Chebyshev polynomials. For reasons of efficiency, the nonlinear convection terms are evaluated pseudo-spectrally in physical space using fast Fourier transforms: the corresponding aliasing errors from the evaluation of the nonlinear terms are removed by the 3/2-rule in the wall-parallel x/z plane. In the wall-normal direction, it has been chosen to increase resolution rather than to use polynomial dealiasing. The time is advanced using a standard four-step low-storage third-order Runge–Kutta method for the nonlinear forcing terms, and a second-order Crank–Nicolson method is employed for the linear terms. The code is fully parallelized for efficient use on both shared and distributed-memory systems.

In order to correctly account for the downstream growth of the boundary layer of the crossflow, a spatial technique is necessary. This requirement is combined with the periodic boundary conditions in the streamwise direction by adding a fringe region, similar to that described by Bertolotti et al. [8], see also Nordstrom et al. [31]. In this region, located at the downstream end of the computational box, the flow is forced to a desired solution $\mathbf{v}$ through the forcing [10],

$$F(\boldsymbol{u}) = \lambda_f(x)(\mathbf{v} - \boldsymbol{u}). \tag{2.3}$$

The desired in- and outflow velocity vector $\mathbf{v}$ may depend on the three spatial coordinates and time. It is smoothly changed from the laminar boundary-layer profile at the beginning of the fringe region to the prescribed inflow velocity vector. In this case, this is chosen as the laminar Blasius boundary-layer profile, but may also contain desired inflow disturbances. The fringe function $\lambda_f(x)$ is identically zero inside the physically relevant domain, and raises smoothly to order one inside the fringe region. The length of the region with $\lambda_f > 0$ is about 20% of the complete domain length. Note that due to the spatially developing boundary layer there is weak positive transpiration throughout the physical domain, and negative wall-normal velocity in the fringe region to fulfill global mass conservation. In the spanwise direction, periodic boundary conditions are used, in accordance with the Fourier discretization in that direction.

The computational domain is a rectangular box containing the boundary layer of the crossflow. Owing to the spectral discretization method employed, it is not directly possible to adapt the computational grid in such a way to include a discretized model of the jet nozzle in the flat plate. The jet discharging into the crossflow boundary layer is, therefore, modeled by imposing inhomogeneous boundary conditions of the wall-normal v velocity component on the flat plate, leaving the no-slip conditions on u and w intact. This simplified model, of course, does not allow for any interaction of the crossflow with the nozzle. The results of e.g., Yuan et al. [37]; Muppidi and Mahesh [28] highlight the importance of including the nozzle to allow for e.g., separation within the pipe. It was also shown by Kelso et al. [22] that the saddle point in the front part of the jet is moving up and down, a motion which might be reduced or even inhibited by the neglect of the pipe. In addition, the fixed boundary condition at $y = 0$ does not allow for any adjustment of the jet profile at that vertical position to the incoming crossflow (in particular a downstream deflection of the profile). On the other hand, as will be shown below, the present simulation captures all the different flow phenomena and vortex systems observed in other simulations and experiments. However, the relative significance of these systems to the overall dynamics might be slightly changed due to the chosen inflow condition. We believe that the underlying main physical mechanisms responsible for the generation and development of the vortex systems are correctly captured in our model.

On the flat plate, homogeneous boundary conditions for the wall-parallel velocity components, u and w, are prescribed, corresponding to the no-slip boundary condition. The main parameters of the jet are the position of the center of the jet orifice $(x_{\text{jet}}, z_{\text{jet}})$, the jet diameter D and the inflow ratio

$$R = \frac{v_{\text{jet}}}{U_\infty} \tag{2.4}$$

of the centerline velocity v_{jet} and the crossflow velocity U_∞. The jet discharging into the crossflow is imposed by a wall-normal velocity

$$v(r, y = 0) = R(1 - r^2) \exp(-(r/0.7)^4), \tag{2.5}$$

with r being the distance from the jet center $(x_{\text{jet}}, z_{\text{jet}})$, normalized by half the jet diameter D,

$$r = (2/D)\sqrt{(x - x_{\text{jet}})^2 + (z - z_{\text{jet}})^2}. \tag{2.6}$$

This inflow profile corresponds to a (laminar) parabolic velocity profile of the pipe flow, smoothened with a super-Gaussian function to allow for an efficient treatment with the spectral discretization of the simulation code. This smoothing slightly increases the radial gradient of the profile, leading to a more pointy appearance than a true parabolic profile. This might be interpreted as the applied profile having a slightly smaller diameter than the one used in the normalization. Note also that the wall-normal velocity component v corresponds to the inflow ratio R in the jet center, and is less than $10^{-5}R$ for $D/2 > 1.276$. For the boundary condition given in Eq. 2.5, the relation between the maximum and the bulk velocity in the center of the jet is approximately 3.

Although physically the boundary layer is assumed to extend to an infinite distance from the wall, the discretization requires a finite domain. Therefore, an artificial boundary condition is applied in the free-stream at wall-normal position L_y via a Neumann condition

$$\left.\frac{\partial \boldsymbol{u}}{\partial y}\right|_{y=L_y} = \left.\frac{\partial \mathbf{v}}{\partial y}\right|_{y=L_y}. \tag{2.7}$$

Far away from the wall, the wall-normal derivative of the base flow $\mathbf{v}$ is vanishingly small, which together with incompressibility approaches $u(x, y = L_y) \approx U_\infty$.

2.2 Data base and parameters

The parameters used for the present simulation cases are described next. The computational domain has a total streamwise length $L_x = 75$, width $L_z = 30$, and height $L_y = 20$ in units of the displacement thickness of the crossflow boundary layer at the domain inlet δ_0^*. The Reynolds number is set to $Re_{\delta_0^*} \equiv \delta_0^* U_\infty/\nu = 165$, with U_∞ being the free-stream velocity of the crossflow. The jet is characterized by the same viscosity as the

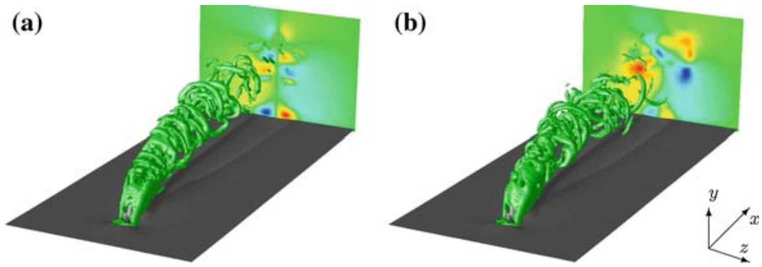

Fig. 1 Instantaneous snapshots of cases **a** DNS-SYM and **b** DNS-ASYM at $t = 700$. The vortical structures are visualized by means of isocontours of constant $\lambda_2 = -0.09$ (*green*); the *gray* contour depicts the streamwise velocity component $u = 0.2$ near the flat plate. The symmetry properties of the flow in the outflow plane are highlighted by color shading according to the spanwise velocity component. (Color figure online)

crossflow, and its inflow ratio (based on the centre velocity) is specified as $R = 3$ according to Eq. 2.4. The jet center is located $L_x\delta_0^*/8$ downstream of the inflow plane. In order to further define the problem setup, the diameter of the jet D is related to the boundary layer thickness as $D/\delta_0^* = 3$. These parameters are in the same range as e.g., the ones considered by Kelso et al. [22]. Compared to Yuan et al. [37], the Reynolds number for this study $Re_D = U_\infty D/\nu = 500$ and the inflow ratio R are lower. However, we employ resolved spectral DNS as a tool, and do not rely on a subgrid-scale model. All computations were performed with a resolution of $(N_x, N_y, N_z) = (256, 201, 144)$ collocation points in physical space. The adequacy of the resolution has been checked by considering Fourier spectra and requiring a sufficient decay of the energy for small scales. Owing to the dense distribution of the Chebyshev collocation points close to the wall and the strong wall-normal velocity component, the time step had to be chosen rather small $\delta t \approx 3 \times 10^{-4}$.

This data base consists of two long DNS runs, each initiated from laminar crossflow fluid (Blasius boundary layer), with the jet smoothly starting to emerge from the wall at $t = 0$. In a first case (denoted DNS-SYM), the simulation at time $t = 0$ does not contain any disturbances apart from the laminar, two-dimensional crossflow boundary layer and the jet boundary condition. The spanwise symmetry of the inflow condition about the plane $z = 0$ is therefore maintained in the whole domain for all $t > 0$, even after the jet breaks up into smaller vortices. In a second run (case DNS-ASYM), an asymmetric disturbance is superimposed upstream of the jet nozzle at $t = 0$, quickly triggering non-symmetric breakup of the jet. In this case, the downstream part of the jet is always asymmetric, although the initial disturbance has long convected out of the domain. Both of these simulations were run up to $t = 700$, corresponding to about 14 flow-through times of the crossflow fluid. The jet reaches a statistically stationary state after about $t = 100$, corresponding roughly to two flow-through times. All the analyses discussed hereafter will be based on snapshots of the flow obtained for times $150 \le t \le 700$. Two instantaneous snapshots of the flow for the two cases, DNS-SYM and DNS-ASYM, are shown in Fig. 1. In this figure, the vortical motion in the jet is visualized by the negative λ_2 vortex-identification criterion [21], highlighting the complex, unsteady flow patterns characteristic for the jet in crossflow. The different spanwise symmetries of the flow for the cases DNS-SYM and DNS-ASYM are apparent in the outflow plane, which is color-coded according to the spanwise velocity component.

2.3 Steady flow and mean flow

In a first step, the time-invariant flow structures are studied. The steady part of the flow is important to be characterized in some detail to get a better understanding of the time-dependent oscillations and distortions developing around the steady flow. Two different possibilities to obtain such a time-invariant flow field have been considered. First, a straight-forward time-average is performed for the period $150 \le t \le 700$ by a weighted sum of all the snapshots recorded with spacing $\Delta t = 1$. This mean flow, however, is in general not a pointwise solution to the governing steady Navier–Stokes equations, but rather to the Reynolds-averaged Navier–Stokes equations, including Reynolds-stress contributions $\langle u_i u_j \rangle$. The mean flow provides the most accurate description of the flow in an averaged sense, i.e., what would be observed experimentally in the mean. It is interesting to note that both the cases DNS-SYM and DNS-ASYM lead to essentially the same mean flow, although their instantaneous representation is different (see Fig. 1).

On the other hand, a true steady solution fulfilling the steady Navier–Stokes equations without additional Reynolds-stress terms can be obtained using the selective frequency damping (SFD) approach as described by

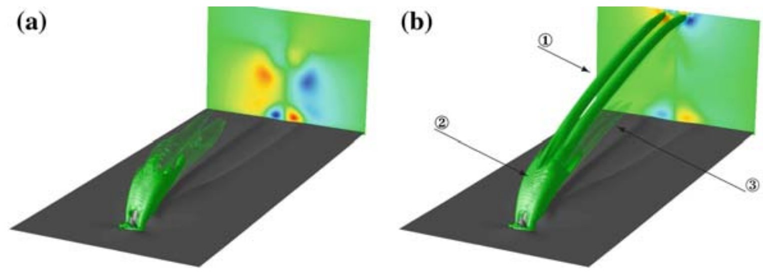

Fig. 2 **a** Mean flow and **b** steady flow obtained by SFD visualized by isocontours of $\lambda_2 = -0.09$ (*solid green*), $\lambda_2 = -0.01$ (*opaque green*), and $u = 0.2$ (*gray*) close to the wall. The vertical plane toward the end of the domain is color coded according to the spanwise velocity component. The numbered labels are discussed in the text. (Color figure online)

Åkervik et al. [1] and applied to the present jet configuration by Bagheri et al. [6]; numerical details and SFD parameters are discussed there. In principle, the SFD adds an explicit forcing term to the governing equations, penalizing any high-frequency disturbances by means of a temporal differential filter. As opposed to the mean flow, this steady flow state represents a true equilibrium solution, which is unstable for the present parameters [6] due to global instability. This flow will, therefore, never be observed in a real situation. The validity of the steady-state solution has been tested numerically by starting a simulation from the steady state without active SFD forcing. The flow eventually became unstable and developed unsteadily; however, the accuracy of the steady state is such that, for about a time span of $\Delta t = 200$, no significant change in the solution is detectable. Thereafter, the instabilities would exponentially grow and eventually lead to similar flow fields as for the cases DNS-SYM and DNS-ASYM, depending on the symmetry properties.

3 Flow features

In this section, the flow phenomena associated with the jet in crossflow are examined in more detail based on the present DNS. In particular, the ubiquitous features described in the literature are briefly reviewed and related to observations in the data presented here.

3.1 Steady features

We begin by comparing the various vortex systems observed in a purely steady solution with those appearing in the mean flow. Figure 2 compares a three-dimensional visualization of the mean and steady flow. The steady structures observed for both flows are: (i) the ubiquitous counter-rotating vortex pair (CVP) rising up into the free stream; (ii) a vortex sheet wrapping around the CVP a few jet diameters in the wall-normal direction; (iii) the wall-vortex system (WVS), consisting of the horse-shoe vortex bending around the upstream part of the jet nozzle, and the wall vortices extending for a long distance downstream of the nozzle. The latter vortices are streamwise-oriented, counter-rotating vortices, which can be considered as the extension of the horse-shoe vortices downstream of the jet nozzle. These features have been described in many publications for the mean flow, see e.g. [15,22,33,37], and they are present in both the steady-state solution and the mean flow in very similar form. The most significant differences are located further away from the wall, indicating that the mean flow distortion due to fluctuations is small in the near-wall region. Most obvious is the clearly stronger, longer, and higher-reaching CVP in the steady flow, indicated by the label ① in Fig. 2. This can be explained by the missing breakup of the vorticity, which leads to a lower momentum loss for the jet fluid, thereby allowing the jet to retain its wall-normal velocity for a longer duration. Since the mean flow is a solution to the RANS equations, it exhibits increased momentum diffusion due to the Reynolds stresses.

A closer inspection of the region close to the jet nozzle (Fig. 2) shows that up to approximately two jet diameters from the wall, a continuous vortex sheet is present on the windward side of the jet (label ②). Referring back to Fig. 1, this vortex sheet is also clearly visible; Lim et al. [25] termed this layer as cylindrical shear layer.At this wall-normal position, the leeward side of the jet already shows the deformation of the jet cross section into the kidney shape characteristic of the growing CVP [29]. An area of negative streamwise velocity is located in the same region, indicating that the roll-up of the sides is sucking in fluid from the downstream part of the crossflow. Above approximately three jet diameters, a two-layer structure of the growing CVP becomes

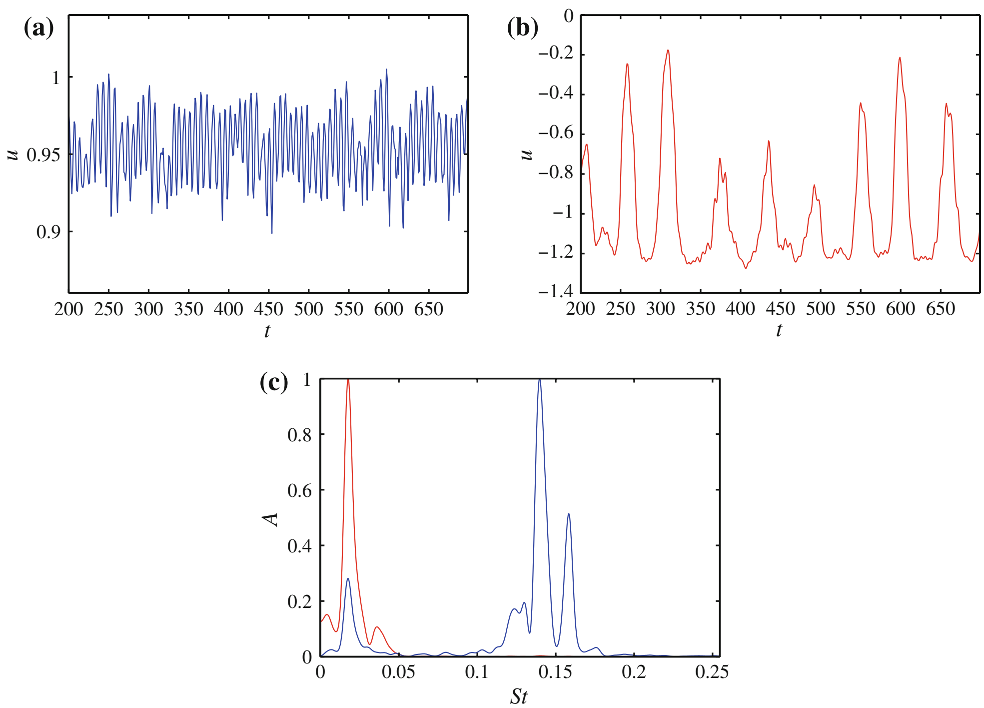

Fig. 3 **a**, **b** Time signals, and **c** power spectra of two probes in the flow. The *red line* corresponds to a probe located in the separated region downstream of the jet, $(x, y, z) = (10.7, 1, 0)$, the *blue line* corresponds to a probe in the shear layer $(x, y, z) = (12, 6, 2)$. (Color figure online)

apparent. The outer vortex shell is detaching from the main CVP direction, forming two distinct vortex cores pointing in the downstream direction and forming a second set of CVP, denoted *lower CVP*, label ③. The inner vortices continue to extend to higher wall-normal distances; now as distinct counter-rotating vortices forming the dominant far-field CVP labeled ①. Note that the direction of rotation is the same on each side of the axis of symmetry for the CVP and lower CVP, i.e., directed in such a way that fluid is lifted up in between the vortices. Although the distinction between the two CVPs is most clear in the steady solution, they can also be identified in the mean flow, Fig. 2a, indicating that their respective dynamics are also present in the time-dependent flow.

These results show that for the development of a counter-rotating vortex pair, the pipe below the jet nozzle is not necessary. This is in agreement with the studies by Cortelezzi and Karagozian [12] and Muppidi and Mahesh [29] who—with different numerical methods and degrees of complexity—obtain a CVP in their simulations without modeling the inflow pipe. In addition, the steady state clearly shows that for the development of a CVP only a steady flow is necessary. To what extent the periodic roll-up of the shear layer might further contribute to the circulation in the CVP [22] can, of course, not be answered by considering the steady solution; however, it seems certain that this roll-up is not the origin of the CVP.

3.2 Unsteady features

In addition to the steady features, a number of unsteady motions are characteristic of the jet in crossflow. Most dominant are the shear-layer vortices, appearing predominantly on the upstream side of the jet trajectory for the given inflow ratio [22,25]. These half-ring-shaped vortices grow, and quickly break down into a series of smaller vortices, which continue to convect downstream and eventually dissipate due to viscosity. The origin and evolution of these vortices have been described and documented by many sources, e.g. [9,15,22,25,30]. These vortices can be seen in the visualizations in Fig. 1 for both the symmetric (DNS-SYM) and asymmetric case (DNS-ASYM). The time signal recorded by a probe located in the shear layer is shown in Fig. 3a for case DNS-ASYM together with its power spectrum. The peak frequency beats with a Strouhal number $St \equiv fD/V_{\text{jet}} = 0.14$ (Fig. 3c). This frequency will be denoted St_2 in the following. In the case of DNS-SYM, which is restricted to symmetric motion about the plane with $z = 0$, a slightly higher Strouhal number, $St = 0.17$ [6] is found. It is interesting to note that this slight difference in frequency for the symmetric and

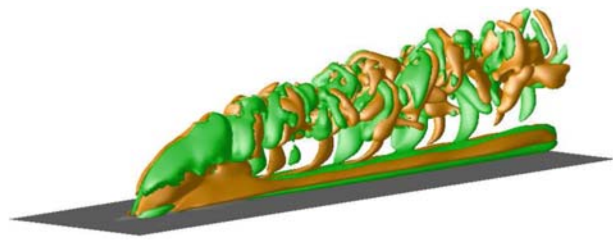

Fig. 4 Isocontours of the wall-normal vorticity for case DNS-ASYM ($\omega_2 = \pm 0.1$), *orange* isocontours correspond to positive, and *green* to negative values. (Color figure online)

asymmetric shear-layer motion is also captured in the linear global stability analysis (see Ref. [6] and Sect. 5 below), which yields $St = 0.19$ and $St = 0.17$ for the symmetric and asymmetric global modes, respectively (denoted S_1 and S_3 in Bagheri et al. [6]).

From visualizations, it is also apparent that the symmetric case leads to more regular flow patterns after the vortex breakdown; the arising vortex structures clearly resemble those documented by Cortelezzi and Karagozian [12]. In the asymmetric case, the basic mechanism of vortex generation in the shear layer is still present; however, the arising flow structures are not as clear as in the symmetric case. In addition, the visual density of the visualized vortices is much higher, indicating a more unstable flow configuration in the unconstrained case.

Another characteristic unsteady feature of the jet in crossflow is the appearance of upright vortices [15,22] in the wake of the jet, connecting the main jet trajectory and the wall vortex system, i.e., the wall vortices. The upright vortices are roughly aligned with the wall-normal direction, periodically shed away from the upstream part of the jet. Several explanations of their origin have been proposed in the literature (see e.g. [22]), including the classical von Kármán-type vortex street. From the results of the DNS data, the upright vortices were identified using isocontours of the wall-normal vorticity ω_2, see Fig. 4 in the case of DNS-ASYM. In the wake, the upright vortices appear regularly with alternating sign of the vorticity. Probes located in the jet wake record exactly the same frequency peak as in the shear layer, i.e., $St_2 = 0.14$. It thus seems that in the flow of this study for each shear-layer vortex, a corresponding upright vortex is created and released. Inspection of an animation clearly confirms this observation, i.e., that the upright vortices are connected to the higher frequency St_2. This physical insight will be further supported below by the global mode analysis.

In addition to this high frequency St_2, there is a clear lower frequency present, both in the shear-layer signal as a secondary peak, but being most dominant in a probe located in the recirculation zone downstream of the jet orifice, see Fig. 3b and c. This frequency is measured as $St_1 = 0.017$. The additional frequency peaks in Fig. 3c are all linear combinations of St_1 and St_2, corresponding to higher harmonics triggered by nonlinear interactions between the two main frequencies.

Several additional time signals from other probes have been obtained and compared to the ones presented here, and in all of these the two frequencies St_1 and St_2 appear as the two dominant fundamental frequencies. In particular, in a probe upstream of the orifice close to the horseshoe vortex, a clearly dominating energy peak at St_1 is recorded. In probes located far downstream, a much broader spectrum is obtained, however, still being dominated by St_1 and St_2. This shows that owing to nonlinearity, the region between the discrete frequencies is gradually filled up as the jet vortices decay into smaller eddies.

4 The separated region

There is some evidence [17] and numerous studies [2,4,7,16,26,34,35] that connect self-sustained oscillations in fluid systems with large unsteady separated regions. The flow under investigation here has two regions of reversed flow: a smaller, essentially steady separated region upstream of the jet which coincides with the horseshoe vortex, and a larger unsteady region of reversed flow directly downstream of the emerging jet near the wall.

4.1 Analysis of the steady near-field

Figure 5a shows the 2D steady flow in the center-plane $z = 0$ in the vicinity of the jet nozzle. Note that the mean flow essentially features the same qualitative properties as the steady flow described here. Upstream of the jet

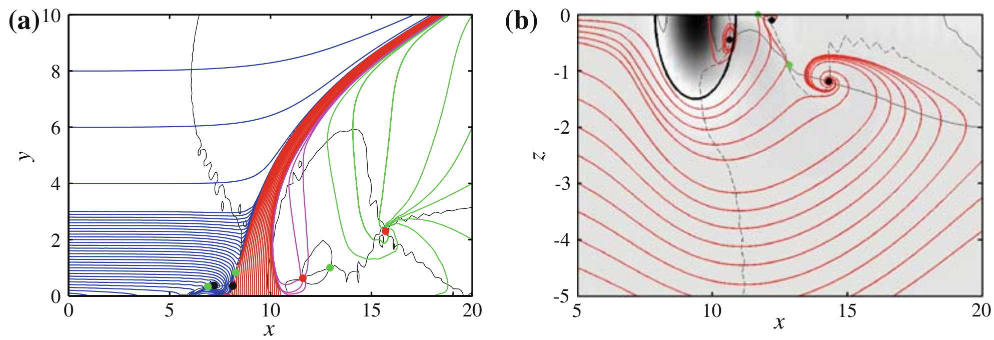

Fig. 5 Two-dimensional cuts of the steady flow, **a** in a $z = 0$ plane, and **b** in a wall-parallel plane close to the wall. The *solid black lines* correspond to zero streamwise velocity $u = 0$, and the *dashed black lines* to $v = 0$. Saddle points are indicated by *green dots*, nodes with *red dots*, and foci with *black dots*. Streamlines are plotted with *colored lines*. In **b**, the background *gray* shade corresponds to the amplitude of the total velocity $(u^2 + v^2)^{(1/2)}$. (Color figure online)

exit, a stagnation point and a small recirculation zone are observed. On the leeward side, a much larger region with backflow is located; however, interestingly, a small region inside this recirculation zone has again positive u velocity. In this plane, the flow is dominated by the high, slightly deflected, wall-normal velocity due to the emerging jet, and a number of interesting stagnation/saddle points and vortex nodes. The wall-normal velocity component also changes sign from negative in the near-wall region to positive further away. The combination of the sign changes allows to identify three singular points of interest in the downstream part of the jet: Two locations (red dots in Fig. 5a) are characterized by positive divergence; and another constitutes a saddle point (green dot). From the streamlines plotted, it is clear that the jet is entraining crossflow fluid from the leeward side. The node located further downstream at $(x, y) \approx (15.7, 2.3)$ has already been described by Kelso et al. [22] and, in the mean flow obtained from DNS, by Muppidi and Mahesh [28]. As opposed to these references, however, in the present study an additional node location could be identified at $(x, y) \approx (11.6, 0.63)$ inside the recirculation zone on the boundary of the above mentioned hole. In between these two nodes another saddle point can be found. The existence of two nodes in the steady flow further indicates the complex flow physics associated with the downstream region of the jet, and consequently, the various instabilities detected along the jet trajectory.

On the windward side, the dominant horseshoe vortex is located at $(x, y) \approx (7.21, 0.37)$ (black dot), and a second vortex center, located much closer to the jet at $(x, y) = (8.13, 0.35)$, is commonly associated with the hovering vortex [22]. These two vortices have opposite directions of rotation. In addition, two saddle points can be identified: the upper one separating the crossflow fluid from being entrained in the jet and the other being recirculated.

A plan view of the streamlines in a (x, z)-plane close to the wall is shown in Fig. 5b. Three foci are identified: one close to the axis of symmetry ($z = 0$), one on the downstream side of the jet boundary, and—most dominantly—in the wake of the jet at $(x, z) \approx (14.31, -1.19)$. In all these points, negative divergence is present indicating entrainment of fluid directed away from the wall. It is interesting to note that the steady flow features a slightly different layout of the various singular points as sketched by Kelso et al. [22]. In particular, the dominant focus is clearly at the downstream of the jet nozzle, and a secondary focus is present close to the axis of symmetry. This second focus is due to the region with positive streamwise velocity embedded in the larger region of backflow.

4.2 Movement of the separation region

The two recirculation regions described above are also detectable in the instantaneous visualization shown in Fig. 6. The animation of the DNS data shows that the separation region downstream of the jet orifice is highly unsteady. In the upper part of this region, patches of negative u are periodically released with the fundamental frequency $St_2 = 0.14$. This happens at a streamwise position close to the jet exit, at which the shear-layer vortices are not yet developed.

In the animations, also the lower frequency St_1 characteristic of the present setup can be observed. The two snapshots shown in Fig. 6 are separated by $\Delta t = 32$ time units, which is approximately half the period of that lower frequency $St_1 = 0.017$. The visualizations show that the whole recirculation zone downstream of

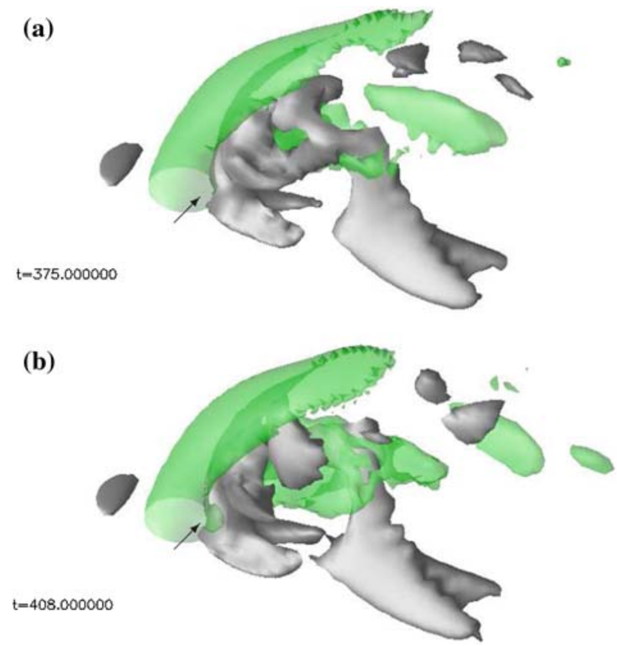

Fig. 6 Instantaneous visualization of the region close to the jet orifice at $t = 376$ and $t = 408$. *Green* isocontours correspond to $v = 0.1$ and *gray* contours to $u = -0.1$. The *arrows* indicate the location of the low-frequency spanwise oscillation of the separation region. (Color figure online)

the jet is periodically moving back and forth in the spanwise direction. The respective positions are indicated in the figure by the arrows. As the probe signals in Fig. 3 show, the low frequency peak is the most dominant just downstream of the jet. The oscillation of the separation region is subsequently felt by the whole jet body and the wake vortex system further downstream. One possible explanation for this motion is given by the comparison of the respective Strouhal number to that of a solid cylinder (see also the corresponding discussion by Fric and Roshko [15] and Ziefle [38] on that topic). For a cylinder wake, the relevant Strouhal number is defined as $St_c = fD/U$ with U being the uniform flow velocity in the far field. Adapting the present definition of the frequency based on the jet velocity gives $St_c = St_1(V_{\mathrm{jet}}/U_\infty)(U_\infty/U)$. Assuming $U/U_\infty \approx 1/3$ due to the reduced streamwise velocity in the proximity of the wall gives $St_c \approx 9St_1 = 0.153$, which is on the same order of magnitude as expected for a solid cylinder. Note that this oscillation is not related to the upright vortices which are associated with the higher frequency St_2 as discussed above.

On the other hand, a careful analysis of the separation region upstream of the jet did not reveal any significant oscillation. In particular, the saddle point upstream of the jet trajectory did not move, which is in contrast to the prediction by Kelso et al. [22]. However, as mentioned earlier, the effect of the chosen inhomogeneous boundary conditions without modeling the inflow pipe might be a factor to explain this apparent difference.

We can thus conclude from observation in our DNS data that the separation region downstream of the jet is in fact oscillating in two directions with two distinct frequencies: A high frequency oscillation in the vertical direction, characterized by periodic shedding with the same frequency as the shear-layer vortices and the upright vortices in the wake, and a lower frequency oscillation, inducing a slow spanwise wiggling of the whole jet and its associated vortex systems.

5 Global modes

The objective of this section is to analyze global modes of the jet in crossflow to gain further insight into the flow dynamics. A global mode is defined as a coherent flow structure (e.g., wavepacket) that exists within the full 3D flow domain. In particular, we focus our attention on two different types of global modes, namely, global eigenmodes and POD modes.

First, we consider the linear subspace spanned by the leading global eigenmodes of the Navier–Stokes equations linearized about the steady-state solution. In this subspace, the behavior of small-amplitude disturbances near the steady solution is captured. More specifically, the eigenmode of the linearized system with the

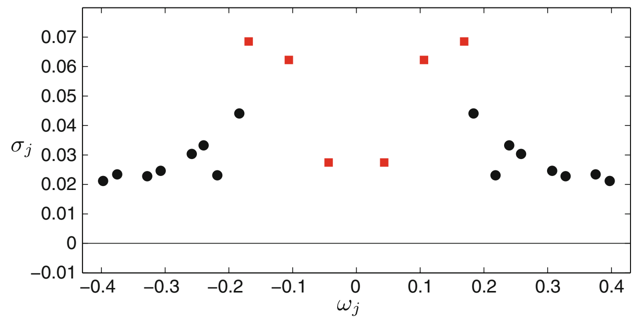

Fig. 7 The linear spectrum of the jet in crossflow at $R = 3$. The eigenvalues marked with *red squares* correspond to anti-symmetric eigenmodes, whereas *black circles* correspond to symmetric eigenmodes. (Color figure online)

largest growth rate determines whether the steady solution is unstable or stable. As established by Huerre and Monkewitz [20]—although this analysis is constrained only to a neighborhood of the steady-state solution—if the baseflow is rendered unstable, then the global (nonlinear) flow may self-sustain global oscillation (e.g., vortex shedding).

Second, we consider the linear subspace spanned by a number of POD modes—the eigenmodes of the spatial correlation matrix. This subspace identifies those parts of the phase space which contains the most kinetic energy, typically attractors in phase space [18]. For the jet in crossflow which we observe as discussed in Sect. 3.2, two fundamental frequencies are associated with two self-sustained global oscillations, indicating a quasi-periodic type of attractor.

5.1 Linear global eigenmodes

The evolution of infinitesimal perturbations $\boldsymbol{u}'(x, y, z, t)$ to a steady solution (e.g., baseflow) $\mathbf{U}(x, y, z)$ is found by inserting $\boldsymbol{u} = \mathbf{U} + \epsilon \boldsymbol{u}'$ and $p = P + \epsilon p'$, where p' is the pressure perturbation, into (2.1) and neglecting terms of order ϵ^2. These equations are solved subject to the same boundary conditions in x, y and z as Eq. 2.1; however, for the perturbation dynamics, the jet boundary condition is not imposed. By enforcing the incompressibility condition and incorporating the boundary conditions, the resulting linearized Navier–Stokes equations (LNS) can be written as initial value problem,

$$\frac{\partial \boldsymbol{u}}{\partial t} = A\boldsymbol{u}, \quad \boldsymbol{u}(t = 0) = \boldsymbol{u}_0. \tag{5.1}$$

In a discretized setting, A is the $n \times n$ Jabobian matrix, where $n = 3n_x n_y n_z$ is the total number of degrees of freedom. If the baseflow is a steady solution, then Eq. 5.1 is autonomous and the eigenmodes of A are of the form:

$$\boldsymbol{u}(x, y, z, t)' = e^{\lambda_j t} \boldsymbol{\phi}_j(x, y, z), \quad j = 1, \ldots, n \tag{5.2}$$

where both the eigenvalues λ_j and eigenmodes $\boldsymbol{\phi}_j$ are complex functions. The eigenmode $\boldsymbol{\phi}_j$ grows or decays in time with a rate given by of $\sigma_j = \mathrm{Re}(\lambda_j)$ and oscillates with temporal frequency given by the $\omega_j = \mathrm{Im}(\lambda_j)$.

If the eigenmodes depend on two or three spatial coordinates, then they are called global eigenmodes to differentiate them from local stability analysis. In our fully 3D case, $n \approx 10^7$, and, therefore, the eigenmodes of A have to be computed using an iterative algorithm (e.g., Arnoldi method) in combination with matrix-free methods. This time-stepper technique is described in Bagheri et al. [5,6]. Linear global stability analysis of two-dimensional steady base flows has only recently become standard in field of hydrodynamics stability (see e.g. [2,3,7,16,34] among others).

In Fig. 7, the linear spectrum is shown. The spectrum was computed using 1,800 snapshots to obtain 22 eigenmodes with smaller residual error than 10^{-7}; see also Bagheri et al. [6]. The eigenvalues, the properties of the corresponding eigenmodes, and their residuals are listed in Table 1. All the computed modes are unstable, and each mode $\boldsymbol{\phi}_j$ is associated with an instability, evolving near to the steady-state baseflow.

Table 1 The properties of each linear global eigenmode

Mode	Growth-rate (σ)	Frequency (St)	Residual	Symmetry	Vortex type
1	0.0685	0.169	10^{-13}	A	Shear/upright
2	0.0622	0.106	10^{-13}	A	Shear/upright
3	0.0441	0.183	10^{-9}	S	Shear
4	0.0333	0.23	10^{-9}	S	Shear
5	0.0303	0.25	10^{-9}	S	Shear
6	0.0274	0.043	10^{-8}	A	Wall
7	0.0246	0.30	10^{-13}	S	Shear
8	0.0233	0.32	10^{-13}	S	Shear
9	0.0230	0.218	10^{-7}	S	Shear
10	0.0227	0.375	10^{-13}	S	Shear
11	0.0211	0.40	10^{-13}	S	Shear

'A' refers to anti-symmetric modes and 'S' to symmetric modes

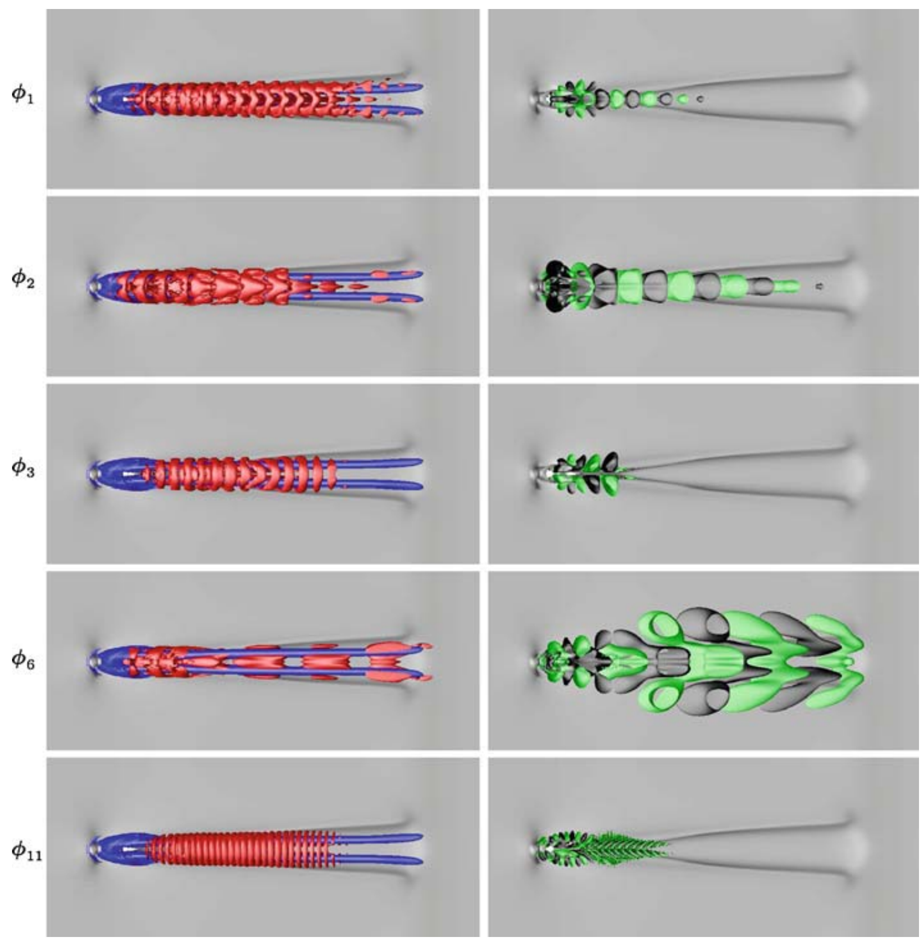

Fig. 8 Five linear global eigenmodes of the jet in crossflow shown from top view. The left column displays contour levels of the λ_2 criterion, whereas the baseflow is shown in *blue* (λ_2) and *gray* (u). The right column shows the structure of the modes near the wall with positive (*black*) and negative (*green*) contours of the w component. The growth rate of the modes decrease from the top to bottom. Modes shown on rows 1, 2, and 4 are anti-symmetric, whereas row 3 and 5 show high-frequency symmetric modes. (Color figure online)

5.1.1 Anti-symmetric modes

The most unstable mode ($\boldsymbol{\phi}_1$) is an anti-symmetric mode (symmetry refers to the u and v component with respect to the z-axis) as shown with red λ_2 contours in Fig. 8a. In the figure, the base flow is shown in blue (λ_2) and gray (u). This mode oscillates with $St = 0.169$. Although the most dominant feature of this instability is

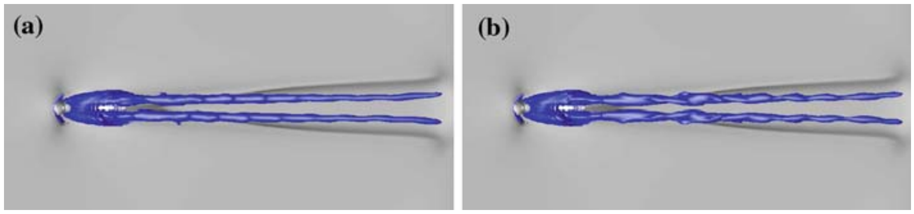

Fig. 9 Top view of the superposition of the base flow and **a** the most unstable global mode, and **b** the most unstable symmetric mode. (Color figure online)

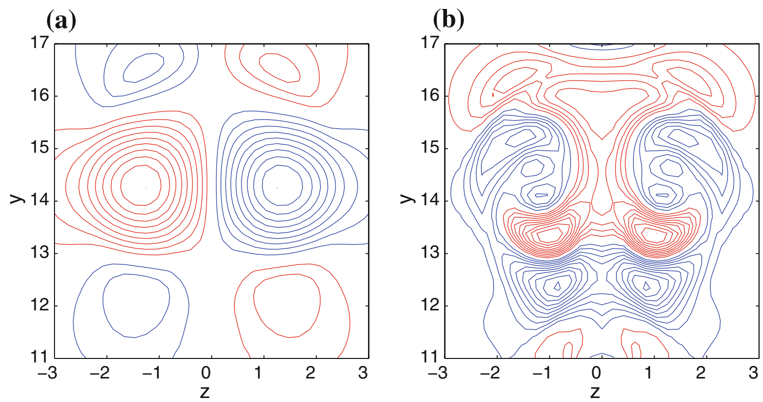

Fig. 10 Streamwise vorticity at $x = 40$ for the steady base flow (**a**), and the most unstable mode (**b**). Contour levels are 0.1, 0.2, …, $1.0 \times \omega_{z,\max}$, *red* is positive; *blue* is negative. (Color figure online)

a wavepacket located on and around the CVP, it is also associated with the upright vortices; we could observe (see Fig. 5b in Bagheri et al. [6] where the same mode from a different angle is shown) a significant spatial structure on the leeward side of the CVP, extending toward the wall in a nearly normal direction to the CVP. The connection of these two vortex systems was also observed in the nonlinear DNS simulation. The amplitude of the mode very close to the wall is significantly smaller compared to the amplitude on the jet as shown in Fig. 8b, where isocontours of the spanwise velocity component are plotted. The alternating positive and negative spanwise velocities in the streamwise direction contribute mainly to the wall-normal vorticity which constitute the upright vortices. In a linear approximation, the structures of the global mode in the jet region, wake region, and wall region grow with the same rate and oscillate with the same frequency. The various vortex systems are thus coupled, which illustrates the global character of the flow. The second most unstable mode ($\boldsymbol{\phi}_2$) is also anti-symmetric, with a very similar spatial structure as the first mode as shown in Fig. 8c and d. However, this mode oscillates with a lower frequency ($St = 0.1$) and is characterized by a somewhat larger spatial wavelength than $\boldsymbol{\phi}_1$. The global eigenmode ($\boldsymbol{\phi}_6$) with the lowest frequency $St = 0.043$ (anti-symmetric) is shown in Fig. 8g and h. Its structure is mostly concentrated close to the wall, and has a rather small amplitude along the CVP. In particular, the structure near the wall is considerably different compared to the other modes. This mode is associated with the shedding of vortices from the spanwise oscillation of the separated region discussed earlier—reminiscent of the global mode of the cylinder wake [16].

In order to gain a better insight into how the instability affects the flow, we superimpose on the steady solution the most unstable anti-symmetric mode with a chosen amplitude such that the modulation caused by the instability becomes clear. As shown in Fig. 9a, the most unstable mode modifies mainly the CVP; a sinuous in-phase oscillation of the two vortex tubes is observed in top view whereas a side view (not shown) reveals out-of-phase oscillations of the tubes. Moreover, the wavelength of the modulation due to the instability seems to be of the same order as that of the vortex cores of the CVP. These can be interpreted as being due to the traits of a short-wavelength instability of a vortex pair as observed during numerical simulation of Laporte [23] and the experiments of Leweke [24]. Such an instability is due to a resonance between two waves of one vortex and straining field induced by the other vortex. In Fig. 10, the streamwise vorticity component in a cross plane (yz-plane) far downstream is shown for the base flow and the most unstable global mode. The CVP centered around $y = 14$ can clearly be seen in Fig. 10a. The global mode, Fig. 10b, shows a characteristic two-lobe structure in each CVP vortex. This is remarkably similar to the vorticity computed analytically for the elliptic instability ([36], Fig. 2) and the short-wave instability ([24], Fig. 10).

These observations suggest (see also [9]) that part of the globally unstable mode is an instability of elliptic type due to a strained vortex. However, in order to fully confirm an elliptic instability, the CVP tubes have to be analyzed locally similar to the analysis described in Fabre et al. [14], which is not within the scope of this article. Previous investigations [23,24] show that at the nonlinear phase—when the amplitude of the short-wave instability has reached sufficiently large amplitude—transverse vortical structures are created between and around the vortex pair. The late stage of these vortical structures (see e.g., Fig. 10 in [23]) are somewhat similar to the structures shown in Fig. 1b.

5.1.2 Symmetric modes

A number of the computed global modes (modes $\boldsymbol{\phi}_3 - \boldsymbol{\phi}_5$, $\boldsymbol{\phi}_7 - \boldsymbol{\phi}_{11}$ in Table 1 and marked with black circles in Fig. 7) represent symmetric shear-layer modes with a rather high temporal frequency. The most unstable symmetric mode is shown in Fig. 8e, f and the symmetric mode with the highest frequency is shown in Fig. 8i and j. The common feature of the symmetric modes is that they have very small spatial support near the wall (see Fig. 8f, j). The global mode consists of a symmetric spanwise oriented row of vortex loop that wrap around the upper part of the CVP and are gradually stretched, and develop "legs" that align with the direction of CVP tubes; the direction of rotation in the loop at $z = 0$ is clockwise viewed in negative z direction. Figure 9b shows the superposition of the baseflow and the most unstable symmetric global mode. The CVPs are modulated in varicose fashion viewed from top. Note that the wavelength of the symmetric instability is rather small compared to the wavelengths commonly observed in the Crow instability [13] of a vortex pair. From a nonlinear simulation of the disturbance (not shown here), we could observe that, as the disturbance grows in amplitude, "arches" are created, i.e., the vortex loops coil up around the upper side of the CVP and their bases join with the CVP. This type of symmetric structures have been observed in many studies (see e.g. [12,22,25]), and have been associated with the roll-up of the cylindrical vortex sheet (shear layer) emerging from the jet nozzle. The symmetric vortex arches observed in the unstable symmetric global modes could thus be partly a result of the Kelvin–Helmholtz roll-up at the upstream side of the jet column. The cylindrical vortex sheet undergoes various stretching and folding processes at the same time as the roll-up, resulting in significantly more complicated structures on the lee side (rear) of the shear layer.

5.1.3 Connection to separated region

Global instabilities are commonly associated with a region in the flow where there is a separation which induces vortex shedding [7,35]. In Sect. 4, two separation regions were identified near the wall: one small steady separation region upstream of the jet orifice, and one separation region just downstream of the jet orifice, oscillating in two directions, slowly in the spanwise direction with $St_1 = 0.017$ and rapidly along the jet trajectory with $St_2 = 0.14$. The Strouhal numbers of the unstable modes are in the range [0.04, 0.17], and do not exactly match the two fundamental shedding frequencies observed in the DNS. However, the stability analysis merely accounts for the linear dynamics in the neighborhood of the steady solution, where the Strouhal numbers can be considerably different from those in the saturated 3D dynamics near the attractor.

It is well known that when the reversed flow in an isolated free shear layer exceeds roughly 15% of the main stream, the flow is absolutely unstable [19]. Although the fully 3D jet in crossflow is considerably more complex, it was shown by Hammond and Redekopp [17] that typical backflow velocities in "realistic" separation bubbles are sufficiently large to induce absolute instability. Absolute instability is a local concept for weakly non-parallel flows and is not straight forward, or perhaps even possible, to conduct such an analysis for the jet in crossflow. However, owing to the fact that globally unstable flows have a region or pocket of local absolute instability somewhere in the flow [11] and that this pocket is connected to a region of significant backflow [17], it is likely that the separated region downstream acts as an oscillator in the flow. It periodically sheds patches of vorticity, which are convected into the jet, wake, and wall region and amplified due to different *local* mechanisms (such as Kelvin–Helmholtz or short-wave elliptic instability). Finally, it should be mentioned that a general feature of absolutely unstable spatially developing flows is that, further downstream, a convectively unstable region follows and finally a stable region. In such flows, the unstable global modes are located far downstream of the absolutely unstable region [20] with the maximum amplitude of the global mode being located in the convectively unstable region. In our setting, the shear layer and CVP could merely act as noise amplifiers. Although the analysis of this study suggests such a scenario, additional local investigation of the steady solution described here should be undertaken to fully ascertain and validate our conjectures.

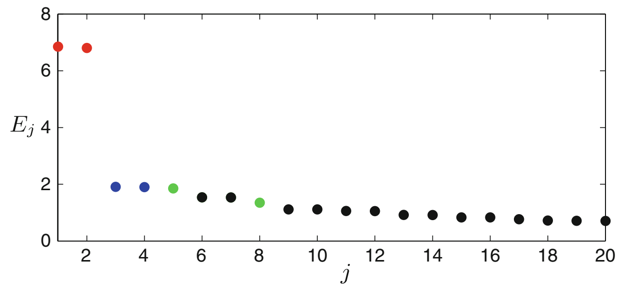

Fig. 11 The energy $E_j = \gamma_j / \sum_i \gamma_i \times 100$ of the POD modes with $j = 1, 20$. The POD modes corresponding to the eigenvalues depicted in color are shown in Fig. 12 whereas the corresponding POD coefficients are shown in Fig. 13. *Red*: antisymmetric high-frequency mode, *blue*: symmetric high-frequency mode, *green*: low-frequency mode. (Color figure online)

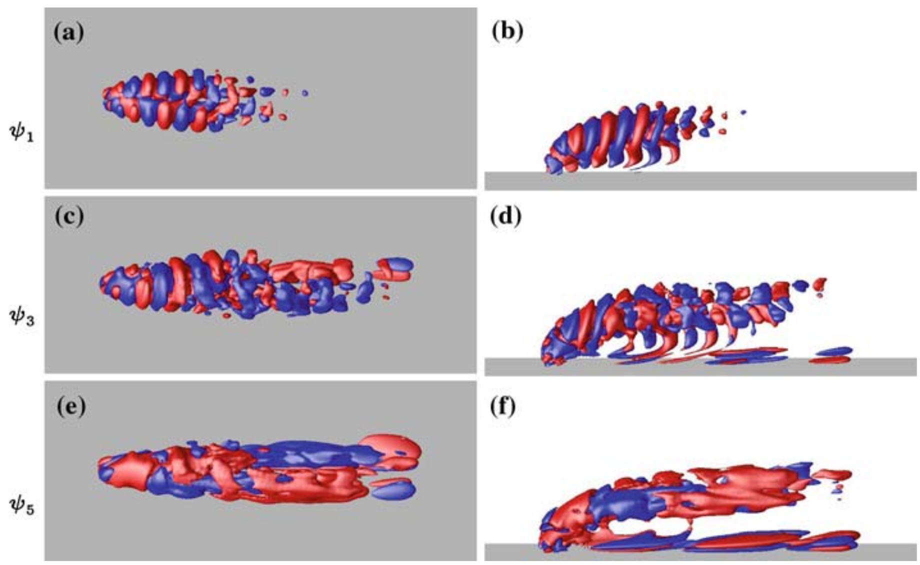

Fig. 12 Positive (*red*) and negative (*blue*) isocontours of the u-velocity component of the three POD modes are shown from top view and side view. The first row corresponds to the modes marked with *red circles*; the second row to those with *blue circles*, and the third row to those with *green circles* in Fig. 11. (Color figure online)

5.2 POD decomposition

Given a set of flow-field snapshots at discrete times $\{\boldsymbol{u}(t_1), \ldots, \boldsymbol{u}(t_m)\}$, the optimal finite-dimensional representation (in the L^2 Hilbert space) of size k of this data set is given by expansion into the first k POD modes [18]. This optimal basis is given by the eigenfunctions $\boldsymbol{\psi}_j$ of the autocorrelation function

$$\left(\int_0^t \boldsymbol{u}(t)\boldsymbol{u}(t)^T \mathrm{d}t \right) \boldsymbol{\psi}_j = \gamma_j \boldsymbol{\psi}_j. \tag{5.3}$$

The eigenfunctions are mutually orthogonal, and the eigenvalues are positive valued, ordered by $\gamma_j \geq \gamma_{j+1}$. Moreover, the eigenvalues γ_j represent twice the kinetic energy in each mode $\boldsymbol{\psi}_j$. The subspace spanning the k POD modes corresponding to the largest k eigenvalues contains the most energetic flow structures in the field. The POD modes can be computed using the method of snapshot [32].

The POD modes of the jet in crossflow were computed using 550 snapshots having equidistant distribution in the time range from $t = 150$ to $t = 700$. The transient flow evolution was hence not included in the data set. All the computed modes satisfy the orthogonality condition down to 10^{-10}. The zeroth mode ($\boldsymbol{\psi}_0$) corresponds to the time-averaged mean flow (shown in Fig. 2) which has been discussed thoroughly earlier.

The energies of the modes $\boldsymbol{\psi}_1 - \boldsymbol{\psi}_{20}$ are shown in Fig. 11, where we clearly notice the pairing of modes, which is typically observed in flows containing traveling structures. Each pair describes the phase and

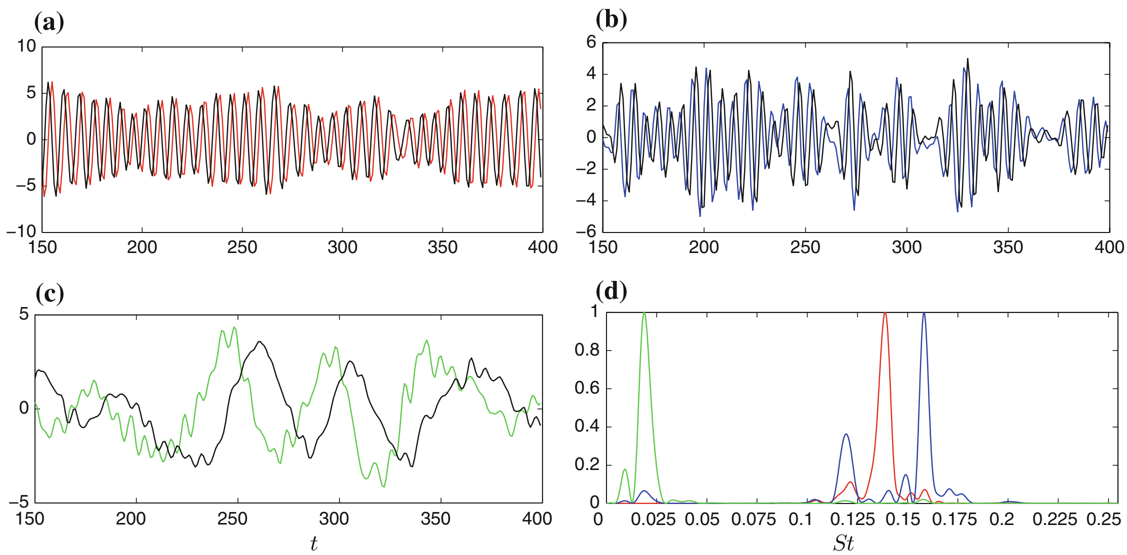

Fig. 13 The temporal behavior of POD modes are shown in terms of the POD coefficients. **a** POD coefficients of the first pair, **b** second pair, and **c** third pair of modes. The power spectra of the signals in (**a**–**c**) are shown in **d**. (Color figure online)

amplitude of one traveling dynamical structure in the flow. The first pair of modes ($\boldsymbol{\psi}_1$, $\boldsymbol{\psi}_2$) contains 68% of the total energy (red circles in Fig. 11). The positive (red) and negative (blue) streamwise velocity components of one mode is shown in Fig. 12a and b from two angles. It clearly displays shear-layer vortices and to some extent the upright vortices. The temporal behavior of this mode is characterized by computing the POD coefficients via a Galerkin projection of the flow-field snapshots onto the mode. The POD coefficient of this pair and its corresponding power spectrum are shown with red lines in Fig. 13a and d, one peak frequency at $St = 0.138$ which matches the Strouhal number of the shedding of the shear-layer vortices observed from DNS ($St_2 = 0.14$). The mode is anti-symmetric and is located mainly near the location where the shedding of the shear-layer vortices takes place. This indicates that the flow mechanism that contributes the most to the total flow energy is the shedding of shear-layer vortices.

The second pair of modes ($\boldsymbol{\psi}_3$, $\boldsymbol{\psi}_4$) contains 1.9% of the total flow energy, with one mode ($\boldsymbol{\psi}_3$) shown in Fig. 12c and d. In contrast to the first pair, this pair has a distinct spatial structure further downstream along the jet trajectory and more pronounced upright vortices on the leeward side. Moreover, anti-symmetric flow structures very close to the wall and far downstream along the flat plate corresponding to wall vortices are also detected. The POD coefficients and the corresponding power spectrum of this pair are shown in Fig. 13b and d, respectively. The signal contains three frequency peaks, where the largest peak is obtained for $St_1 + St_2 = 0.158$ and the second largest is $-St_1 + St_2 = 0.121$, due to the interaction of the two fundamental shedding frequencies.

Finally, we pair up two modes with similar energy levels consisting of modes $\boldsymbol{\psi}_5$ and $\boldsymbol{\psi}_8$, with the energy 1.8 and 1.3%, respectively. Although these modes do not have exactly the same energy, they form a pair as shown by the POD coefficients in Fig. 13c. The corresponding power spectrum of the time signal, Fig. 13d, clearly shows a low-frequency peak with $St = 0.0188$ which nearly matches the shedding frequency $St_1 = 0.017$ (associated with the separation region downstream of the jet orifice and close to the wall). Indeed, as shown in Fig. 12f, this mode has a significant anti-symmetric and large-scale structure near the wall. However, this mode also has structures along the jet trajectory further away from the wall. This indicates that the shedding of wall vortices is coupled to the jet body, i.e., the low frequency can be detected nearly anywhere in the vicinity of the jet since the whole jet is oscillating with that frequency.

6 Discussion and conclusions

We have performed numerical simulations of a jet in crossflow and analyzed two steady and three unsteady vortex systems by means of the time-averaged mean flow and its associated POD modes, as well as the steady solution to Navier–Stokes equations, and its associated linear global eigenmodes.

The results can be summarized as follows:

(i) A steady-state solution of the jet has been analyzed, featuring a dominant counter-rotating vortex pair (CVP), horseshoe, and wake vortices. The CVP is a true steady vortex system, and the associated roll-up of shear-layer vortices is not the origin of the CVP. The steady-state solution also shows that the CVP is composed of an outer shell (shear layer), shielding the inner CVP from the crossflow fluid. The downstream deflection of the outer vortex sheet leads to the formation of a secondary (lower) CVP, composed of swirling fluid of the crossflow. This secondary CVP can be observed for long distances downstream; however, it is weaker than the main (upper) CVP.

(ii) Shear-layer vortices were observed in the nonlinear DNS to be continuously shed with a frequency of $St_2 = 0.14$, initiated by a separation region about one jet diameter along the jet trajectory. This frequency is one of two fundamental frequencies in the flow, as all other frequencies in the flow were found to be higher harmonics of these two. The frequency $St_2 = 0.14$ matches the frequency obtained from the POD analysis $St = 0.138$ for the most energetic mode pair, whereas it is smaller than the Strouhal number 0.169 obtained from the linear global analysis for the most unstable global mode. The leading POD mode and the most unstable linear global eigenmodes are both anti-symmetric coherent structures associated with the shear-layer vortices. In particular, we could identify "two-lobe" structures in the most unstable global mode that are strikingly similar to previous experimental, numerical, and analytical studies of elliptic short-wave instability of a vortex pair. The symmetric unstable modes have "arch-like" structures of vortex loops that are similar to previous studies of the Kelvin–Helmholtz shear-layer roll-up on the upper side of the cylindrical vortex sheet. It remains to be shown whether pockets of absolute instability exist near the separated region, which shed vortices and then grow as they propagate along the CVP. However, we are investigating these issues further using both global and local techniques.

(iii) Upright vortices were observed in the DNS which connect the shear-layer vortices to the wall vortices. The upright vortices are also shed with the shear-layer frequency St_2. The connection of the vortex systems was also confirmed by both the linear and POD analysis, since the shear-layer global modes display significant connected structures on the leeward side of the CVP, oriented in the vertical direction toward the flat plate.

(iv) The second fundamental frequency is the shedding of wall vortices with $St_1 = 0.017$ from a separation region just downstream of the jet nozzle. The spanwise oscillation of the separated region is similar to the von-Kármán vortex street observed behind bluff bodies. The global coherent structures also capture this dynamics. The physical insight gained by an unstable linear global eigenmode showed remarkable similarities with global modes of the wake behind circular cylinder. The POD mode associated with the wall vortices, on the other hand, indicates that the whole jet is oscillating with the low frequency as the coherent mode has non-zero amplitude along the jet trajectory. Similar to high frequency St_2, the shedding frequency in the wall region $St_1 = 0.017$ is very close to $St = 0.0188$ obtained from the POD analysis, but significantly smaller than $St = 0.043$ obtained from the linear global analysis.

Acknowledgments We thank the Swedish National Infrastructure for Computing (SNIC) for allowing us to avail their computer facility. Financial support provided by the Swedish Research Council (VR) is gratefully acknowledged.

References

1. Åkervik, E., Brandt, L., Henningson, D.S., Hœpffner, J., Marxen, O., Schlatter, P.: Steady solutions of the Navier–Stokes equations by selective frequency damping. Phys. Fluids **18**(068102), 1–4 (2006)
2. Åkervik, E., Hœpffner, J., Ehrenstein, U., Henningson, D.S.: Optimal growth, model reduction and control in a separated boundary-layer flow using global eigenmodes. J. Fluid Mech. **579**, 305–314 (2007)
3. Åkervik, E., Ehrenstein, U., Gallaire, F., Henningson, D.S.: Global two-dimensional stability measures of the flat plate boundary-layer flow. Eur. J. Mech. B **27**, 501–513 (2008)
4. Alan, M., Sandham, N.D.: Direct numerical simulation of laminar separation bubbles with turbulent reattachment. J. Fluid Mech. **403**(1), 223–250 (2000)
5. Bagheri, S., Åkervik, E., Brandt, L., Henningson, D.S.: Matrix-free methods for the stability and control of boundary layers. AIAA J. **47**, 1057–1068 (2009)
6. Bagheri, S., Schlatter, P., Schmid, P.J., Henningson, D.S.: Global stability of a jet in cross-flow. J. Fluid Mech. **624**, 33–44 (2009)
7. Barkley, D., Gomes, M.G., Henderson, R.D.: Three-dimensional instability in flow over a backward-facing step. J. Fluid Mech. **473**, 167–190 (2002)

8. Bertolotti, F.P., Herbert, T., Spalart, P.R.: Linear and nonlinear stability of the Blasius boundary layer. J. Fluid Mech. **242**, 441–474 (1992)
9. Blanchard, J.N., Brunet, Y., Merlen, A.: Influence of a counter rotating vortex pair on the stability of a jet in a cross flow: an experimental study by flow visualizations. Exp. Fluids **26**(1), 63–74 (1999)
10. Chevalier, M., Schlatter, P., Lundbladh, A., Henningson, D.S.: Simson—A Pseudo-Spectral Solver for Incompressible Boundary Layer Flows. Tech. Rep. TRITA-MEK 2007:07. KTH Mechanics, Stockholm, Sweden (2007)
11. Chomaz, J., Huerre, P., Redekopp, L.: A frequency selection criterion in spatially developing flows. Stud. Appl. Math. **84**, 119–144 (1991)
12. Cortelezzi, L., Karagozian, A.R.: On the formation of the counter-rotating vortex pair in transverse jets. J. Fluid Mech. **446**, 347–373 (2001)
13. Crow, S.C.: Stability theory for a pair of trailing vortices. AIAA J. **8**, 2172–2179 (1970)
14. Fabre, D., Cossu, C., Jacquin, L.: Spatio-temporal development of the long and short-wave vortex-pair instabilities. Phys. Fluids **12**(5), 1247–1250 (2000)
15. Fric, T.F., Roshko, A.: Vortical structure in the wake of a transverse jet. J. Fluid Mech. **279**, 1–47 (1994)
16. Giannetti, F., Luchini, P.: Structural sensitivity of the first instability of the cylinder wake. J. Fluid Mech. **581**, 167–197 (2007)
17. Hammond, D.A., Redekopp, L.G.: Local and global instability properties of separation bubbles. Eur. J. Mech. B **17**(2), 145–164 (1998)
18. Holmes, P., Lumley, J., Berkooz, G.: Turbulence Coherent Structuresm Dynamical Systems and Symmetry. Cambridge University Press, Cambridge (1996)
19. Huerre, P., Monkewitz, P.A.: Absolute and convective instabilities in free shear layers. J. Fluid Mech. **159**, 151–168 (1985)
20. Huerre, P., Monkewitz, P.: Local and global instabilities in spatially developing flows. Annu. Rev. Fluid Mech. **22**, 473–537 (1990)
21. Jeong, J., Hussain, F.: On the identification of a vortex. J. Fluid Mech. **285**, 69–94 (1995)
22. Kelso, R.M., Lim, T.T., Perry, A.E.: An experimental study of round jets in cross-flow. J. Fluid Mech. **306**, 111–144 (1996)
23. Laporte, F., Corjon, A.: Direct numerical simulations of the elliptic instability of a vortex pair. Phys. Fluids **12**(5), 1016–1031 (2000)
24. Leweke, T., Williamson, C.H.K.: Cooperative elliptic instability of a vortex pair. J. Fluid Mech. **360**(1), 85–119 (1998)
25. Lim, T.T., New, T.H., Luo, S.C.: On the development of large-scale structures of a jet normal to a cross flow. Phys. Fluids **13**(3), 770–775 (2001)
26. Marquillie, M., Ehrenstein, U.: On the onset of nonlinear oscillations in a separating boundary-layer flow. J. Fluid Mech. **458**, 407–417 (2002)
27. Megerian, S., Davitian, L., Alves, L., Karagozian, A.: Transverse-jet shear-layer instabilities. Part 1. Experimental studies. J. Fluid Mech. **593**, 93–129 (2007)
28. Muppidi, S., Mahesh, K.: Study of trajectories of jets in crossflow using direct numerical simulation. J. Fluid Mech. **530**, 81–100 (2005)
29. Muppidi, S., Mahesh, K.: Two-dimensional model problem to explain counter-rotating vortex pair formation in a transverse jet. Phys. Fluids **18**(085103), 1–9 (2006)
30. Muppidi, S., Mahesh, K.: Direct numerical simulation of round turbulent jets in crossflow. J. Fluid Mech. **574**, 59–84 (2007)
31. Nordström, J., Nordin, N., Henningson, D.S.: The fringe region technique and the Fourier method used in the direct numerical simulation of spatially evolving viscous flows. SIAM J. Sci. Comput. **20**(4), 1365–1393 (1999)
32. Sirovich, L.: Turbulence and the dynamics of coherent structures i–iii. Quart. Appl. Math. **45**, 561–590 (1987)
33. Smith, S.H., Mungal, M.G.: Mixing, structure and scaling of the jet in crossflow. J. Fluid Mech. **357**, 83–122 (1998)
34. Theofilis, V.: Advances in global linear instability analysis of nonparallel and three-dimensional flows. Prog. Aerosp. Sci. **39**, 249–315 (2005)
35. Theofilis, V., Hein, S., Dallmann, U.: On the origins of unsteadiness and three-dimensionality in a laminar separation bubble. Philos. Trans. R. Soc. Lond. A **358**, 3229–3246 (2000)
36. Waleffe, F.: On the three-dimensional instability of strained vortices. Phys. Fluids A **2**(1), 76–80 (1990)
37. Yuan, L.L., Street, R.L., Ferziger, J.H.: Large-eddy simulation of a round jet in crossflow. J. Fluid Mech. **379**, 71–104 (1999)
38. Ziefle, J.: Large-eddy simulation of complex massively-separated turbulent flows. PhD thesis, ETH Zürich, Switzerland, Diss. ETH No. 17846 (2008)